JOURNAL OF COMPUTATIONAL PHYSICS 109, 202–214 (1993)

Computation of Attached Three-Dimensional Turbulent Boundary Layers

A. T. DEGANI AND J. D. A. WALKER

Department of Mechanical Engineering and Mechanics, Lehigh University, Bethlehem, Pennsylvania 18015

Received November 4, 1992

In conventional calculation schemes for turbulent flow near walls, a substantial number of mesh points are required to resolve the intense profile variations in the near-wall region. In the present method, the velocity distribution across the entire wall layer is represented by analytic embedded functions; the outer-layer flow is calculated subject to the condition that the numerical solution blends smoothly into the embedded wall-layer functions. As the computation proceeds downstream, the wall shear stress and the wall skew angle are obtained from algebraic formulae derived from a general asymptotic analysis. It is shown that on the order of a 50% reduction of mesh points may be realized without any degradation in the accuracy of the computed results. The present methodology is very robust and capable of calculating bi-directionally skewed cross-stream velocity profiles.

1. INTRODUCTION

It is well known that attached turbulent boundary layers are double-structured, consisting of a relatively thick, effectively inviscid outer layer and a thin viscous wall layer near the surface. In the calculation of such flows, a highly refined mesh is necessary to resolve the intense gradients in the wall layer, while a relatively coarser mesh is adequate farther away. In typical calculations [1–3], 50% of the total mesh points may be devoted to the wall layer. The central idea in the embedded-function approach is to take advantage of the similarity structure that exists in the wall layer for attached turbulent flows, thereby allowing representation of the velocity profiles across the entire wall layer by analytic embedded functions. The outer-layer flow is calculated by requiring that the numerical solution merge to the correct asymptotic form near the wall layer. The outer-layer numerical solutions and wall-layer embedded functions are then matched asymptotically to obtain composite velocity profiles that are valid across the entire boundary layer, while the wall shear stress is calculated from algebraic relationships obtained as a result of the matching. Because the wall-layer flow is not computed, a considerable saving in storage and an increase in computational efficiency is possible. The method has previously been developed for two-dimensional [4] and plane-of-symmetry [5] turbulent boundary layers; in these situations the embedded-function method utilized about half the mesh points of a conventional calculation procedure (which computes the flow all the way to the wall), with no degradation in accuracy [4, 5]. Note that the embedded-function method bears a similarity to so-called wall-function methods [6], but the implementation of these two methods differs considerably [4].

Here, the embedded-function method is developed for fully three-dimensional flows. Three-dimensional flows are inherently more complicated because, along with the wall shear stress, the wall skew angle must also be obtained as part of the numerical solution. For simplicity, attention will be focused here on incompressible boundary-layer flows, although the methodology has been applied to compressible flows [7] and can, in principle, be utilized with full Navier–Stokes solution methods. Note that the main intent here is to demonstrate the applicability of the embedded-function methodology to three-dimensional flows within the context of a given turbulence model, as opposed to trying to infer a "best turbulence model" through direct comparisons with experimental data.

At this stage, it is useful to delineate the salient features of a three-dimensional boundary-layer flow which is conveniently described in the streamline coordinate system shown in Fig. 1. The streamwise direction x_1 is defined by the external streamline at the boundary-layer edge, and the cross-stream direction x_2 is perpendicular to x_1; the vector $\bar{x} = (x_1, x_2)$ describes a location on the solid boundary. The normal coordinate x_3 completes the orthogonal coordinate system. Due to the curvature of the external streamline, a cross-stream pressure gradient is set up which is positive for the case shown in Fig. 1. As a consequence, the velocity vector rotates from the local external streamline in a direction of decreasing cross-stream pressure gradient as the wall is approached. Therefore, the cross-stream velocity increases

0021-9991/93 $5.00

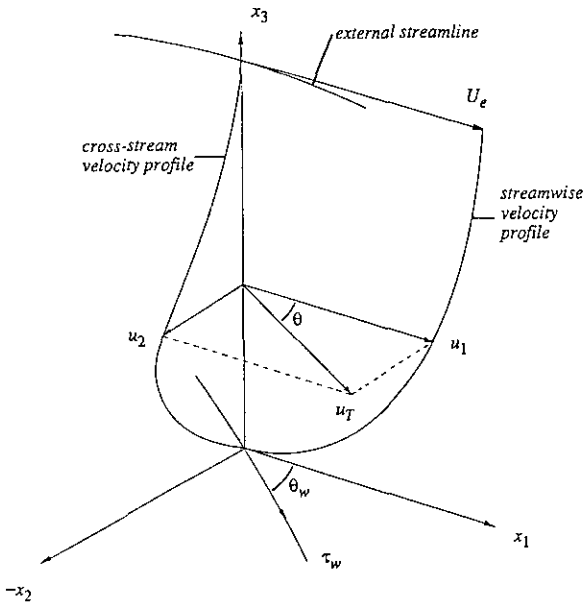

FIG. 1. Schematic of a three-dimensional turbulent boundary layer.

from zero at the boundary-layer edge, reaches a maximum, and then decreases back to zero at the wall to satisfy the no-slip condition. In contrast, the behavior of the streamwise velocity is qualitatively similar to that in a two-dimensional boundary layer. The direction of the limiting streamline at the wall is determined by applying L'Hôpital's rule to the ratio u_2/u_1 as $x_3 \to 0$. In general, the angle between the tangents to the external streamline and the limiting streamline at the wall is nonzero; therefore, the velocity vector rotates through what will be referred to as the wall skew angle. Thus the velocity profile is said to skew and this feature is a distinct characteristic of a three-dimensional boundary-layer flow.

2. GOVERNING EQUATIONS

Consider a three-dimensional turbulent boundary-layer flow in which U^*_{ref} and L^*_{ref} are the representative speed and length, respectively; the Reynolds number is defined as $\text{Re} = U^*_{\text{ref}} L^*_{\text{ref}}/\nu^*$, where ν^* is the kinematic viscosity and is assumed constant. In dimensionless variables, the boundary-layer equations in a streamline coordinate system are as follows [7]: The continuity equation is

$$\frac{\partial}{\partial x_1}(h_2 u_1) + \frac{\partial}{\partial x_2}(h_1 u_2) + h_1 h_2 \frac{\partial u_3}{\partial x_3} = 0, \tag{1}$$

and the x_1- and x_2-momentum equations are given by

$$\frac{u_i}{h_i}\frac{\partial u_1}{\partial x_i} - K_2 u_1 u_2 + K_1 u_2^2 = \frac{U_e}{h_1}\frac{\partial U_e}{\partial x_1} + \frac{\partial \tau_{13}}{\partial x_3}, \tag{2}$$

$$\frac{u_i}{h_i}\frac{\partial u_2}{\partial x_i} - K_1 u_1 u_2 + K_2 u_1^2 = K_2 U_e^2 + \frac{\partial \tau_{23}}{\partial x_3}, \tag{3}$$

respectively. The operator on the left sides of (2) and (3) is

$$\frac{u_i}{h_i}\frac{\partial}{\partial x_i} = \frac{u_1}{h_1}\frac{\partial}{\partial x_1} + \frac{u_2}{h_2}\frac{\partial}{\partial x_2} + u_3\frac{\partial}{\partial x_3}, \tag{4}$$

where h_1 and h_2 are the metric coefficients in the x_1 and x_2 directions, respectively, and K_1 and K_2 are the corresponding curvatures defined by

$$K_1 = -\frac{1}{h_1 h_2}\frac{\partial h_2}{\partial x_1}, \qquad K_2 = -\frac{1}{h_1 h_2}\frac{\partial h_1}{\partial x_2}. \tag{5}$$

In accordance with the usual boundary-layer formulation [7], the metric coefficient in the normal direction h_3 is taken to be unity, and h_1 and h_2 are independent of x_3. The total shear stresses, τ_{13} and τ_{23}, are given by

$$\tau_{13} = \sigma_{13} + \frac{1}{\text{Re}}\frac{\partial u_1}{\partial x_3}, \qquad \tau_{23} = \sigma_{23} + \frac{1}{\text{Re}}\frac{\partial u_2}{\partial x_3}, \tag{6}$$

where σ_{13} and σ_{23} are the dimensionless turbulent shear stresses. Both u_1 and u_2 vanish at the wall and $u_1 \to U_e$, $u_2 \to 0$ at the boundary-layer edge. Note that, once the external flow field is specified, the metric coefficients and the curvatures are all uniquely determined [7].

3. ASYMPTOTIC STRUCTURE

An essential step in the formulation of a rational calculation procedure is a derivation of the appropriate asymptotic structure in the limit of large Reynolds number. In the embedded-function method, the no-slip boundary condition at the wall is to be replaced by asymptotic conditions reflecting a generalized functional form for the velocity components near the wall but still within the outer layer. In addition, alternative formulae must be developed to calculate the wall shear stress and wall skew angle, which are computed in a conventional scheme by evaluating velocity gradients at the wall. Such information can be obtained from a general asymptotic analysis of the three-dimensional turbulent boundary-layer equations [7–9]; the relevant results are briefly summarized in this section.

The friction velocity is defined in terms of τ_w, the nondimensional magnitude of the wall shear stress, by $u_\tau = \sqrt{\tau_w}$; as in two-dimensional boundary layers [10], the ratio u_τ/U_e is small for large Reynolds numbers. The wall

skew angle θ_w scales on the friction velocity in the limit of large Reynolds number [7–9] and a scaled wall skew angle θ_* may be defined by

$$\theta_* = \frac{\tan \theta_w}{u_*}, \qquad u_* = \frac{u_\tau \cos \theta_w}{U_e}. \tag{7}$$

Here u_* is the scaled friction velocity in the local streamwise direction and $u_* \to 0$ while θ_* is $O(1)$ as $\mathrm{Re} \to \infty$. The scaled outer-layer variable η and the wall-layer variable y^+ are defined by

$$\eta = \frac{x_3}{\Delta_o}, \qquad y^+ = \mathrm{Re}\, u_\tau x_3, \tag{8}$$

where Δ_o is a measure of the local boundary-layer thickness and the appropriate specification of Δ_o is discussed in Section 5.

Consider the asymptotic behavior for the velocity distribution first. In the wall layer, both velocity components are small and have the forms [7, 9]

$$u_1 = U_e u_* U^+(y^+) + \cdots, \tag{9a}$$

$$u_2 = U_e u_*^2 \theta_* U^+(y^+) + \cdots, \tag{9b}$$

where the profile function U^+ must vanish at $y^+ = 0$ and conform to the law of the wall

$$U^+ \sim \frac{1}{\kappa} \log y^+ + C_i \qquad \text{as} \quad y^+ \to \infty, \tag{10}$$

at the outer edge of the wall layer. Here κ and C_i are the von Karman and log-law constants (assumed to be 0.41 and 5.0, respectively). Note that the cross-stream velocity in (9) is $O(u_*)$ smaller than the streamwise component. In the outer layer, the appropriate expansions for the velocities are [7, 9]

$$u_1 = U_e \left\{ 1 + u_* \frac{\partial F_1}{\partial \eta} + u_*^2 \frac{\partial F_2}{\partial \eta} + \cdots \right\}, \tag{11a}$$

$$u_2 = U_e u_* \theta_* \left\{ \frac{\partial G_1}{\partial \eta} + u_* \frac{\partial G_2}{\partial \eta} + \cdots \right\}, \tag{11b}$$

where

$$\frac{\partial F_1}{\partial \eta} \sim \frac{1}{\kappa} \log \eta + C_o, \qquad \frac{\partial G_1}{\partial \eta} \sim 1 \qquad \text{as} \quad \eta \to 0; \tag{12a}$$

$$\frac{\partial F_2}{\partial \eta} \sim C_1, \qquad \frac{\partial G_2}{\partial \eta} \sim \frac{1}{\kappa} \log \eta + C_o \qquad \text{as} \quad \eta \to 0. \tag{12b}$$

Here C_o and C_1 are functions of $\bar{x} = (x_1, x_2)$ to be found, which generally depend on the specific outer-layer turbulence model used. With the asymptotic forms in (10) and (12), it may be easily confirmed that the velocities in (9) and (11) match if the condition

$$\frac{1}{u_*} = \frac{1}{\kappa} \log(\mathrm{Re}\, u_\tau \Delta_o) + C_i - C_o - u_* C_1 + \cdots \tag{13}$$

is satisfied; this match condition provides a relation between the outer scale Δ_o and the wall shear stress.

Next, consider the total shear stress. Substitution of (9) and (10) into (2) and (3), along with integration and subsequent evaluation at large y^+, yields [9]

$$\tau_{13} \sim u_\tau^2 \cos \theta_w - \frac{1}{\mathrm{Re}\, u_\tau} \frac{U_e}{h_1} \frac{\partial U_e}{\partial x_1} y^+ \left\{ 1 + u_*^2 \frac{\log^2 y^+}{\kappa^2} \right\} + \cdots \qquad \text{as} \quad y^+ \to \infty, \tag{14a}$$

$$\tau_{23} \sim u_\tau^2 u_* \theta_* \cos \theta_w - \frac{1}{\mathrm{Re}\, u_\tau} K_2 U_e^2 y^+ \times \left\{ 1 + u_*^2 \frac{\log^2 y^+}{\kappa^2} \right\} + \cdots \qquad \text{as} \quad y^+ \to \infty. \tag{14b}$$

Once again, note that the ratio of the cross stream to streamwise shear stress is of $O(u_*)$ to leading order. In the outer layer, the form of the expansions for total shear stresses is suggested by (14) and given by

$$\tau_{13} = u_\tau^2 \cos \theta_w \{ T_1(\bar{x}, \eta) + u_* T_2(\bar{x}, \eta) + \cdots \}, \tag{15a}$$

$$\tau_{23} = u_\tau^2 \theta_* \cos \theta_w \{ \tilde{T}_1(\bar{x}, \eta) + u_* \tilde{T}_2(\bar{x}, \eta) + \cdots \}. \tag{15b}$$

In order to match the asymptotic form in (14), it may be verified [9] that

$$T_1 \sim 1 - 2\beta_s \frac{\eta \log \eta}{\kappa} + \cdots, \qquad T_2 \sim -\beta_s \frac{\eta \log^2 \eta}{\kappa^2} + \cdots \qquad \text{as} \quad \eta \to 0, \tag{16}$$

$$\tilde{T}_1 \sim 2\gamma \frac{\eta \log \eta}{\kappa} + \cdots, \qquad \tilde{T}_2 \sim 1 + \gamma \frac{\eta \log^2 \eta}{\kappa^2} + \cdots \qquad \text{as} \quad \eta \to 0. \tag{17}$$

Here β_s and β_n are pressure-gradient parameters in the streamwise and cross-stream directions, respectively, defined by

$$\beta_s = -\frac{\Delta_o}{U_e u_\tau} \frac{U_e}{h_1} \frac{\partial U_e}{\partial x_1}, \qquad \beta_n = -\frac{\Delta_o}{U_e u_\tau} K_2 U_e^2, \tag{18}$$

and the parameter γ is defined according to

$$\gamma = -\beta_n / \theta_*. \tag{19}$$

It should be emphasized that (7)–(19) are general results independent of a specific turbulence-closure assumption.

4. FORMULATION

For computational convenience, normalized velocities are defined by

$$F=\frac{u_1}{U_e}, \qquad G=\frac{u_2}{U_e}, \tag{20}$$

and a generalization of the two-dimensional streamwise Levy–Lees variable is introduced by [1, 2, 11]

$$\xi_1=\int_0^{x_1} Z_0\,dx_1, \qquad Z_0(x_1)=U_e h_1 h_2^2|_{x_2=0}, \qquad \eta=x_3/\Delta_o, \tag{21}$$

with the cross-stream variable left unchanged so that $\xi_2=x_2$. Although the embedded-function method may be adopted with any self-consistent two-layer turbulence model, a simple algebraic model of the form

$$\sigma_{13}=\bar{\varepsilon}_1\frac{\partial u_1}{\partial x_3}, \qquad \sigma_{23}=\bar{\varepsilon}_2\frac{\partial u_2}{\partial x_3}, \tag{22}$$

is used here (for illustrative purposes), where $\bar{\varepsilon}_1$ and $\bar{\varepsilon}_2$ represent eddy viscosities in the streamwise and cross-stream directions, respectively.

The governing equations (1)–(3) in computational coordinates are then of the form

$$\frac{\partial V}{\partial\eta}+A_1\frac{\partial F}{\partial\xi_1}+A_2\frac{\partial G}{\partial\xi_2}+A_8F+A_9G=0, \tag{23}$$

$$\frac{\partial}{\partial\eta}\left\{\varepsilon_1\frac{\partial F}{\partial\eta}\right\}-V\frac{\partial F}{\partial\eta}-A_1F\frac{\partial F}{\partial\xi_1}-A_2G\frac{\partial F}{\partial\xi_2}+A_3(1-F^2)-A_6G^2=0, \tag{24}$$

$$\frac{\partial}{\partial\eta}\left\{\varepsilon_2\frac{\partial G}{\partial\eta}\right\}-V\frac{\partial G}{\partial\eta}-A_1F\frac{\partial G}{\partial\xi_1}-A_2G\frac{\partial G}{\partial\xi_2}+A_4(1-F^2)-A_7G^2-(A_3-A_5)FG=0, \tag{25}$$

where V is defined by

$$V=\frac{\Delta_o^2U_e}{h_1}\left\{\frac{h_1}{U_e\Delta_o}u_3+\frac{\partial\eta}{\partial x_1}F+\frac{h_1}{h_2}\frac{\partial\eta}{\partial x_2}G\right\}. \tag{26}$$

The coefficients A_1–A_9 are given in the Appendix. The outer-layer length scale Δ_o is determined at each location in a manner to be described in Section 5. In addition, ε_1 and ε_2 denote the total viscosities in each of the streamwise and cross-stream directions, respectively, with

$$\varepsilon_i=\bar{\varepsilon}_i+\mathrm{Re}^{-1}, \qquad i=1,2, \tag{27}$$

and the total stresses are given by

$$\tau_{13}=\varepsilon_1\frac{\partial u_1}{\partial x_3}, \qquad \tau_{23}=\varepsilon_2\frac{\partial u_2}{\partial x_3}. \tag{28}$$

In the external streamline coordinate system, the boundary conditions at the edge are

$$F\to 1, \qquad G\to 0 \qquad \text{as} \quad \eta\to\infty. \tag{29}$$

The performance of the embedded-function method will be compared with a typical conventional method [1, 2, 11] whose main features are summarized here. The boundary-layer integrations are started in laminar flow and here the appropriate normal variables are

$$\bar{\eta}=\frac{U_e h_2}{\sqrt{2\xi_1}}\sqrt{\mathrm{Re}}\,x_3, \qquad \bar{V}=\sqrt{\mathrm{Re}}\,V. \tag{30}$$

In the full-calculation scheme [1, 2, 11], computations are performed all the way to the wall, where the no-slip condition requires

$$F=G=0 \qquad \text{at} \quad \bar{\eta}=0. \tag{31}$$

A simple formula capturing the essence of a Cebeci–Smith eddy-viscosity turbulence model [12] is used here. In the outer layer, close to the boundary-layer edge,

$$\varepsilon_1=\varepsilon_2=U_e\,\delta^*K, \qquad K=0.0168, \tag{32a}$$

and in the inner region,

$$\varepsilon_1=\varepsilon_2=\kappa^2x_3^2D^2\sqrt{(\partial u_1/\partial x_3)^2+(\partial u_2/\partial x_3)^2}+\frac{1}{\mathrm{Re}}, \tag{32b}$$

where κ is the von Karman constant and D is the Van Driest damping factor given by

$$D=1-\exp\left(-\frac{y^+}{26}\right). \tag{33}$$

The quantity δ^* in (32a) is defined by

$$\delta^*=\int_0^\infty\{1-\sqrt{F^2+G^2}\}\,dx_3, \tag{34}$$

so that its value is rotationally invariant in a three-dimensional flow.

Now consider the embedded-function method. To facilitate comparison, a similar model to (32) is adopted; however, since calculations are now performed only in the outer layer, an inner-region model is no longer necessary. A simple choice for an outer-layer model that is consistent with the asymptotic structure described in Section 3 and with (32) is

$$\varepsilon_i = U_e \delta^* \begin{cases} K, & \eta > \eta_m, \\ \dfrac{\kappa\eta}{\eta_*}, & \eta \leqslant \eta_m, \end{cases} \tag{35}$$

for $i = 1, 2$ where

$$\eta_* = \frac{U_e \delta^*}{\Delta_o u_\tau}, \qquad \eta_m = \frac{K\eta_*}{\kappa}. \tag{36}$$

The models (32) and (35) are the same in each coordinate direction and are said to be isotropic; the validity of such an assumption has sometimes been questioned (see, for example, the discussion in Ref. [9]), although an isotropic model appears to be desirable for the wall layer [9]. In principle, a nonisotropic model for the outer region could easily be adopted by choosing different values for the outer-layer constant K in the streamwise and cross-stream directions. Because the intent of the present study is to demonstrate embedded-function methodology within the context of a general class of turbulence models rather than address the issue of the best turbulence model, isotropic models (32) and (35) are used here for simplicity; as discussed in Ref. [9], such models yield a wall-layer flow which is collateral to leading order in the limit as $\mathrm{Re} \to \infty$.

Once a turbulence model is adopted, the asymptotic behavior of the velocity components may be refined to include effects of pressure gradient in the limit of small η. Substitution of (15)–(17), (20), (35), and (36) into (28) with subsequent integration gives

$$F \sim 1 + u_* \left\{ \frac{1}{\kappa} \log \eta + C_o - 2\beta_s \frac{\eta \log \eta}{\kappa^2} + \cdots \right\} + u_*^2 \left\{ C_1 - \beta_s \frac{\eta \log^2 \eta}{\kappa^3} + \cdots \right\} + \cdots \quad \text{as} \quad \eta \to 0, \tag{37}$$

$$G \sim u_* \theta_* \left\{ 1 + 2\gamma \frac{\eta \log \eta}{\kappa^2} + \cdots \right\} + u_*^2 \theta_* \left\{ \frac{1}{\kappa} \log \eta + C_o + \gamma \frac{\eta \log^2 \eta}{\kappa^3} + \cdots \right\} + \cdots \quad \text{as} \quad \eta \to 0. \tag{38}$$

The formulas in (37) and (38) represent refined versions of the asymptotic forms in (11) and (12) to include pressure-gradient terms near the surface; this refinement is only possible, in general, once a specific turbulence-closure assumption is made.

5. NUMERICAL PROCEDURE

First consider the procedure adopted to determine Δ_o, the outer-layer length scale. Let η_2 denote the value of η at the first mesh point off the wall in the embedded-function method (see Fig. 2). From (8), the wall variable y^+ is related to η by

$$\eta = y^+ \frac{1}{u_\tau \Delta_o \mathrm{Re}}. \tag{39}$$

Let y_m^+ denote the value of y^+, where the matching of the outer-region numerical solution to the embedded function takes place. In the present study, y_m^+ was chosen to be approximately equal to 120. In practice, the specific value of y_m^+ used in the calculation has no effect on the performance of the method or on the results, provided y_m^+ is large. However a larger value of y_m^+ yields enhanced savings in the number of mesh points used. By insisting that the match take place at a constant value of both y^+ and η at all streamwise and cross-stream locations, the outer-layer length scale may be conveniently defined from (39) according to

$$\Delta_o = \frac{y_m^+}{\eta_2} \frac{1}{u_\tau \mathrm{Re}}, \tag{40}$$

as in the two-dimensional application of the method [4]. The important advantage of using (40) to determine Δ_o is

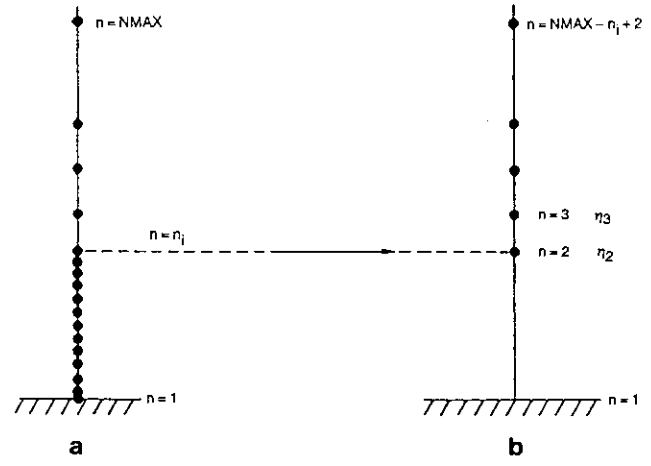

FIG. 2. Schematic representation of the change in the mesh: (a) original mesh at $\xi_1 = \xi_{1,m-1}$; (b) new mesh after switch at $\xi_1 = \xi_{1,m}$.

that the mesh for η is identical at all locations (ξ_1, ξ_2) within the boundary layer.

Next, consider the boundary conditions. In addition to (29), conditions near the surface are provided by the asymptotic results (37) and (38) for small η. Let f_2 and f_3 denote values of F at the locations η_2 and η_3, where η_3 denotes the second point from the wall. Since both η_2 and η_3 are small, (37) may be used to represent F at these two locations and therefore

$$f_3 - f_2 = \frac{u_*}{\kappa} \log\left(\frac{\eta_3}{\eta_2}\right) - 2\beta_s u_* \left\{\frac{\eta_3 \log \eta_3 - \eta_2 \log \eta_2}{\kappa^2}\right\} - \beta_s u_*^2 \left\{\frac{\eta_3 \log^2 \eta_3 - \eta_2 \log^2 \eta_2}{\kappa^3}\right\}. \tag{41}$$

The advantage of this point–slope representation for small η is that the unknown functions C_o and C_1 do not appear in (41). Similarly, for the cross-stream velocity, from (19) and (38),

$$g_3 - g_2 = \frac{u_*^2 \theta_*}{\kappa} \log\left(\frac{\eta_3}{\eta_2}\right) + 2\gamma u_* \theta_* \left\{\frac{\eta_3 \log \eta_3 - \eta_2 \log \eta_2}{\kappa^2}\right\} + \gamma u_*^2 \theta_* \left\{\frac{\eta_3 \log^2 \eta_3 - \eta_2 \log^2 \eta_2}{\kappa^3}\right\}, \tag{42}$$

where g_3 and g_2 are the values of G at η_3 and η_2, respectively. Finally, upon substitution of (37) and (38) into the continuity equation (23), it may be shown that

$$V \sim -\eta \left\{A_1 \frac{\partial F}{\partial \xi_1} + A_2 \frac{\partial G}{\partial \xi_2} + A_8 F + A_9 G\right\} \quad \text{as} \quad \eta \to 0, \tag{43}$$

and this relation is used to evaluate V at η_2 in terms of η_2, f_2, g_2, as well as the streamwise and cross-stream gradients, which are computed using simple backward differences. By using values obtained from the previous iterate, the right-hand side of these equations may be evaluated. In a general iterative procedure at any streamwise location, estimates of u_* and θ_* from the previous iteration are used to evaluate the right sides of (41) and (42); these relations are readily incorporated [7] into a solution algorithm for the difference approximations to (23)–(25).

In the full-calculation method [1, 2], the initial profiles used for the velocity are self-similar laminar solutions at a leading edge or along a line of attachment of the external flow. The calculations are then continued in the downstream direction through the laminar and transitional regions into the fully turbulent zone. For the transitional region, a simple model due to Dhawan and Narasimha [1, 13] was used. The present embedded-function method pertains to a fully developed turbulent flow, and here the full-calculation method is used to supply initial velocity profiles within the fully turbulent zone just downstream of the end of transition. The calculation is switched from the full-calculation method at station $\xi_{1,m-1}$ to the embedded-function method at $\xi_{1,m}$ as suggested schematically in Fig. 2.. An initial value of Δ_o must be specified along each external streamline and a convenient choice is

$$\Delta_o = \frac{\delta^*}{u_*} \quad \text{at} \quad \xi_1 = \xi_{1,m-1}, \tag{44}$$

which is the outer length scale associated with self-similar solutions [7–9]. This choice for Δ_o fixes η_2 at the initial station along each external streamline (for a selected value of y_m^+) and subsequent values of Δ_o downstream are computed from (40). At the switchpoint $\xi_{1,m-1}$, the new mesh in η is determined from the definitions of η and $\bar{\eta}$ given by (8) and (30), respectively; this gives

$$\eta = \bar{\eta} \sqrt{2\xi_1/\mathrm{Re}}\, (1/U_e h_2 \Delta_o), \tag{45}$$

where Δ_o is obtained from (44). All original points below $\eta = \eta_2$ are no longer needed and are discarded as indicated schematically in Fig. 2.

In general, some conditions are also required in the cross-stream direction. The flow configurations used in this study contain a plane of symmetry, and it is useful to outline the special approach used there. Denoting the symmetry plane by $x_2 = 0$, G vanishes there but the quantity G', defined as

$$G' = \frac{1}{U_e h_2} \frac{\partial u_2}{\partial x_2}\bigg|_{x_2=0} = \frac{1}{h_2} \frac{\partial G}{\partial x_2}\bigg|_{x_2=0}, \tag{46}$$

does not. The solution develops independently of the rest of the boundary layer along $x_2 = 0$ and, by taking $G = 0$, the special forms of the continuity and the streamwise equations (1) and (2) are easily obtained; the cross-stream equation is obtained from (3) by noting that $G \sim x_2 h_2 G'$. In this manner G' replaces G as the unknown in the cross-stream momentum equation; the resulting equations are similar to the full three-dimensional case (see the Appendix). The plane-of-symmetry solution procedure [5] is similar to that for the full three-dimensional flow. Near the symmetry plane $\beta_n \sim x_2 h_2 \beta_n'$ and $\theta_* \sim x_2 h_2 \theta_*'$. If g_3' and g_2' denote the values of G' at η_3 and η_2, respectively, it is readily inferred that a numerical approximation to the asymptotic boundary condition for G' is given by (42), with g_3, g_2, and θ_* replaced with their primed counterparts. On the symmetry plane, the parameter γ is now given by

$$\gamma = \lim_{x_2 \to 0} \left\{-\frac{\beta_n}{\theta_*}\right\} = -\frac{\beta_n'}{\theta_*'}. \tag{47}$$

The numerical method used [2, 7] for the outer layer is second-order accurate in $\Delta\eta$ and first-order accurate in $\Delta\xi_1$ and $\Delta\xi_2$. The solution is advanced in a step-by-step manner in the ξ_1 direction; for the cross-stream equation (25), a simple forward or backward difference [7] is used for $\partial G/\partial\xi_2$, depending on the sign of G at that mesh point. At a given station (ξ_1, ξ_2), a direct solution of the difference equations produces current estimates of F, G, and V across the entire boundary layer and values of the skin friction u_τ and wall skew angle θ_w are obtained iteratively as follows. The asymptotic forms for F and G for small η are given by (37) and (38), but both C_o and C_1 are unknown at this stage. However, by using the velocity-match condition given by (13), the values of F and G at η_2 may be written as

$$f_2 \simeq u_* \left\{\frac{1}{\kappa}\log y_m^+ + C_i\right\} - u_*\beta_s \frac{\eta_2 \log \eta_2}{\kappa^2} \times \left\{2 + \frac{u_*}{\kappa}\log \eta_2\right\}, \tag{48a}$$

$$g_2 \simeq u_*^2\theta_* \left\{\frac{1}{\kappa}\log y_m^+ + C_i\right\} - u_*\beta_n \frac{\eta_2 \log \eta_2}{\kappa^2} \times \left\{2 + \frac{u_*}{\kappa}\log \eta_2\right\}. \tag{48b}$$

The pressure-gradient parameters defined by (18) are evaluated using the previous estimate of u_τ and Δ_o; consequently, new estimates of u_* and θ_* are evaluated directly from (48) and u_τ and θ_w are obtained from (7). This procedure is a nested iteration and is repeated until convergence is obtained; in practice, one pass is usually adequate at each station.

The quantity δ^* appears in the turbulence model (cf. (32) and (35)) and hence must be evaluated at each iteration. The definition of δ^* in (34) may be expanded as

$$\delta^* = (\mathrm{Re}\, u_\tau)^{-1} \int_0^{y_m^+} \{1 - \sqrt{F^2 + G^2}\}\, dy^+ + \Delta_o \int_{\eta_2}^{\infty} \{1 - \sqrt{F^2 + G^2}\}\, d\eta, \tag{49}$$

where the first and second integrals represent contributions to δ^* from the wall and outer layers, respectively. With the definition of F and G in (20) and the wall-layer expressions for the velocity components in (9), (49) gives

$$\delta^* = (\mathrm{Re}\, u_\tau)^{-1} \left\{y_m^+ - u_* \int_0^{y_m^+} U^+\, dy^+ + \cdots\right\} + \Delta_o \int_{\eta_2}^{\infty} \{1 - \sqrt{F^2 + G^2}\}\, d\eta, \tag{50}$$

where the first integral is accurate to $O(u_*^2)$ and the second is obtained numerically from the current estimates of the outer-layer velocity profile distributions. For the wall-layer model for U^+ adopted in this study, the first integral in (50) may be approximated by its asymptotic form for large y_m^+ and is given by [4, 10]

$$\int_0^{y_m^+} U^+\, dy^+ \sim \frac{y_m^+}{\kappa}\{\log y_m^+ - 1\} + C_i y_m^+ - 66.9. \tag{51}$$

With the current estimates of u_τ, θ_w, and δ^*, the boundary conditions in (41)–(43) are reevaluated and the turbulence model updated; the iterative procedure, at each station and along each line of constant ξ_1, is continued until convergence is realized.

A composite profile for the streamwise velocity u_1 is obtained in the usual way by adding the outer- and wall-layer solutions and subtracting out the common contribution according to

$$\frac{u_1}{U_e} = u_* U^+(y^+) + F(\eta) - u_* U_c, \tag{52}$$

where U_c is the common contribution expressed in terms of the wall-layer variable by

$$U_c = \frac{1}{\kappa}\log y^+ + C_i. \tag{53}$$

The numerical solution F is known only for $\eta \geqslant \eta_2$, but for small η, F may be continued analytically into the wall layer by using the asymptotic form (37). Using (13), (37), and (52), it is easily shown that the velocity for $\eta < \eta_2$, or, equivalently, for $y^+ < y_m^+$ may be written

$$\frac{u_1}{U_e} = u_* \left\{U^+(y^+) - \beta_s \frac{\eta \log \eta}{\kappa^2}\left\{2 + \frac{u_*}{\kappa}\log \eta\right\}\right\}, \quad \eta < \eta_2. \tag{54}$$

This representation is valid for large y^+ but is also a reasonable [7] approximation across the wall layer; a higher-order term (reflecting the influence of pressure gradient) is needed to complete the wall-layer solution [7]. In a similar way, the composite profile for u_2 is

$$\frac{u_2}{U_e} = u_*^2\theta_* U^+(y^+) + G(\eta) - u_*^2\theta_* U_c, \tag{55}$$

for values of $\eta \geqslant \eta_2$. On the other hand, for $\eta < \eta_2$, G is

replaced by the asymptotic form given in (38) which results in the approximate representation in the wall layer:

$$\frac{u_2}{U_e} = u_* \theta_* \left\{ u_* U^+(y^+) + \gamma \frac{\eta \log \eta}{\kappa^2} \left\{ 2 + \frac{u_*}{\kappa} \log \eta \right\} \right\}, \quad \eta < \eta_2. \tag{56}$$

Note that representations (54) and (56) are utilized in this study only to plot the results very close to the wall. Finally, a formal composite construction for the total streamwise and cross-stream shear stresses is not necessary since these quantities are regular at the wall and are obtained directly from (15)–(17).

6. RESULTS AND DISCUSSION

The embedded-function method has been applied to the calculation of the turbulent boundary-layer flow for a number of external flows [7]; here, results are presented for the situation having a symmetry plane shown in Fig. 3, where a boundary layer on a flat surface encounters a wedge shape. An analytical solution for the external flow is easily obtainable for this example and details regarding the calculation of the metrics and curvatures are given elsewhere [7]. Calculations were carried out for several sets of mesh sizes as a check on the accuracy, but for the results reported here, a uniform mesh is chosen to discretize the wall surface with 101 and 21 mesh points along the streamwise and cross-stream directions, respectively. Thus calculations were carried out along 20 individual external streamlines outboard of the plane of symmetry. In the full-calculation method, for the normal variable $\bar{\eta}$, a "telescoping" mesh-point system is chosen, viz.,

$$\bar{\eta}_n = \bar{\eta}_{n-1} + \alpha(\bar{\eta}_{n-1} - \bar{\eta}_{n-2}), \qquad n = 3, n_{\max}, \tag{57}$$

with

$$\bar{\eta}_2 - \bar{\eta}_1 = 0.001, \qquad \alpha = 1.041, \qquad n_{\max} = 210. \tag{58}$$

All reference quantities are evaluated at the upstream leading edge of the flat plate and the working medium is assumed to be air. Upstream conditions are assumed to be given by $p^*_{\text{ref}} = 2117$ lbf/ft^2 and $T^*_{\text{ref}} = 600°$ R; using the perfect gas law and the Sutherland relation [14], the corresponding density and absolute viscosity are $\rho^*_{\text{ref}} = 0.0662$ lbm/ft^3 and $\mu^*_{\text{ref}} = 1.345 \times 10^{-5}$ lbm/ft s. The reference velocity and length are chosen to be $U^*_{\text{ref}} =$ 600 ft/s, $L^*_{\text{ref}} = 10$ ft, and this yields a Reynolds number of $\text{Re} = 2.96 \times 10^7$. Transition is assumed to begin and end at streamwise Reynolds numbers $\text{Re}_x = \text{Re}\, U_e x_1$ of 5×10^5 and 1.5×10^6, respectively. The embedded-function algorithm is then initiated at the upstream edge of the fully turbulent zone, but both schemes are continued to enable comparison of the calculated results. Consequently, the embedded-function results are shown from $x_1 \geq 0.35$ which is the approximate location of the end of transition. The

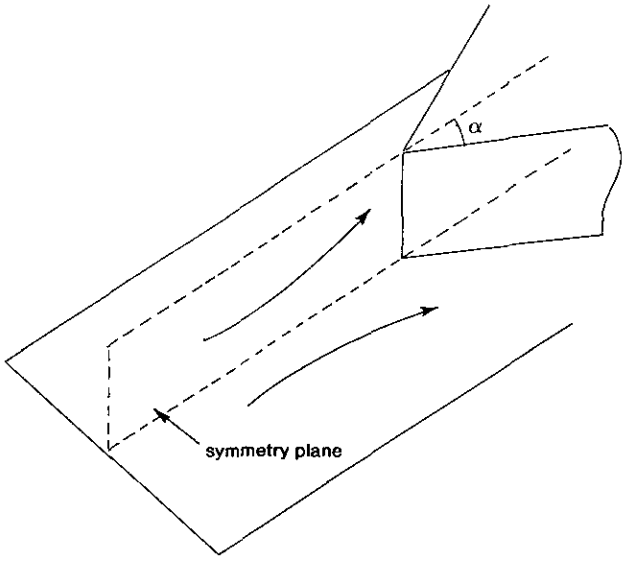

FIG. 3. Schematic of a flow configuration consisting of a flat plate with an attached vertical-wedge half-angle $\alpha = 30°$ located farther downstream.

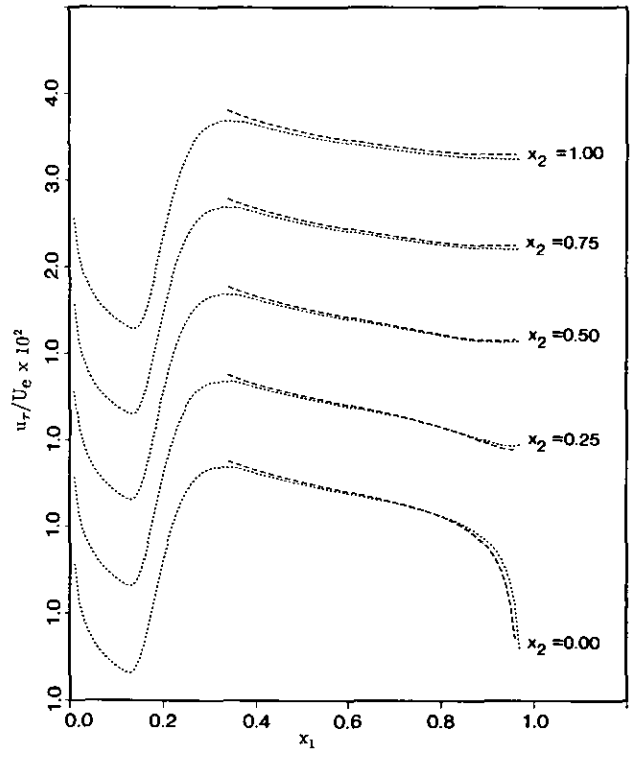

FIG. 4. Streamwise variation of the friction velocity for the wedge flow for five selected cross-stream locations: ··· full calculation; – – – embedded-function.

match point is located at $y_m^+ = 123$ ($\eta_2 = 0.015$), and in terms of the original mesh, the match point is located at $\bar{\eta}_{90}$. Consequently, the total number of mesh points is decreased by 43% by using the embedded-function method.

For convenience, the full-calculation and the embedded-function methods will subsequently be referred to by FC and EF, respectively. Figure 4 shows the friction velocity as a function of x_1 for various cross-stream locations. Note the staggered ordinate, which will be used in all subsequent figures describing the variation of a calculated quantity with respect to (x_1, x_2). Both schemes fail to converge at $(x_1 \simeq 0.95, x_2 = 0)$. Beyond this point, backflow is expected and it is generally not possible to continue a marching solution of the boundary-layer equations without utilizing interactive theory (see, for example, Ref. [15]); furthermore, the asymptotic structure described in Section 3 is not expected to apply within such a flow regime. Composite velocity profiles spanning the entire thickness of the boundary layer were constructed in the EF method from (52)–(56). The streamwise velocity profiles produced by both methods were found to be virtually identical. Selected cross-stream velocity profiles are shown in Fig. 5, where y^+ is the abscissa. Recall that the match point is located at $y_m^+ = 123$. The computed profiles compare very well for large y^+, but a slight discrepancy between the two sets of results may be noted deep within the wall layer where $y^+ \sim O(1)$. This is simply a reflection of the approximate nature of formula (56) for $y^+ = O(1)$. Figure 6 shows a plot of the logarithm of the wall skew angle measured in radians with respect to (x_1, x_2). At the leading edge of the flat plate, the flow is nominally two-dimensional; however, as the wedge is approached, θ_w increases rapidly and the mean flow becomes increasingly three-dimensional. The results in Figs. 4 and 6 indicate a good agreement in u_τ and θ_w between both calculation methods. Figures 7 and 8 show the total streamwise and cross-stream shear stresses at five selected locations. It is evident from Fig. 7 that τ_{13} is constant across the wall layer, but close examination of Fig. 8 appears to suggest that τ_{23} is not constant for $y^+ \lesssim 120$. In particular, for the plot P_5 the value at $y^+ = 120$ is about half the value at the wall. Although $\tau_{23} = \text{const}$ in the wall layer is asymptotically valid in the limit $\text{Re} \to \infty$, Fig. 8 shows that the higher-order effects of pressure gradient are not negligible at the large but finite Reynolds number under consideration. For higher Reynolds numbers, the plots in Fig. 8 would be similar but the abscissa $y^+ = 100$, for example, would shift progressively to the left and the asymptotic result $\tau_{23} = \text{constant}$ for $y^+ \leqslant 100$ would be realized.

Previous investigators (see, for example, Ref. [16]) have suggested that the velocity vector is aligned with the direction of the wall shear stress across the entire wall layer (i.e.,

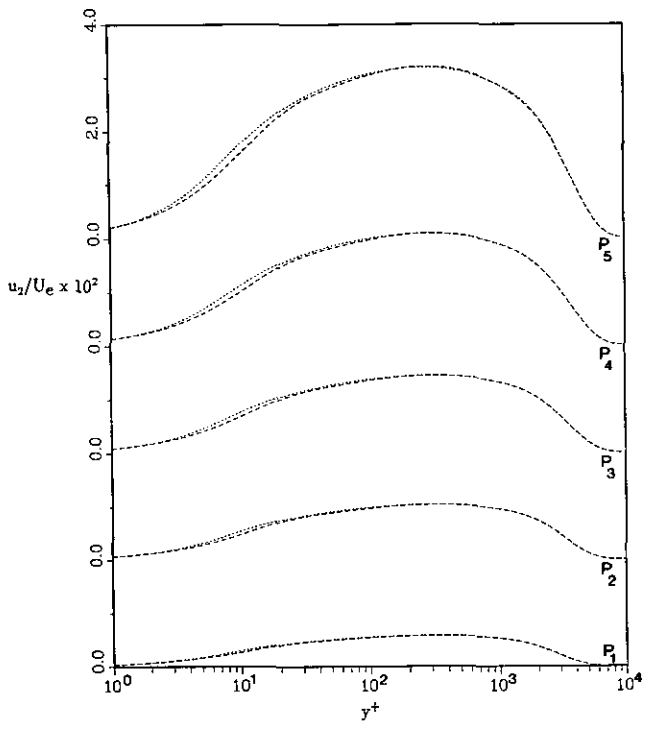

FIG. 5. The cross-stream velocity profile at five selected locations for the wedge flow: ··· full calculation; – – – embedded function. All cross-stream locations are $x_2 = 0.25$. The x_1 locations are: $P_1, x_1 = 0.6$; $P_2, x_1 = 0.7$; $P_3, x_1 = 0.75$; $P_4, x_1 = 0.8$; $P_5, x_1 = 0.85$.

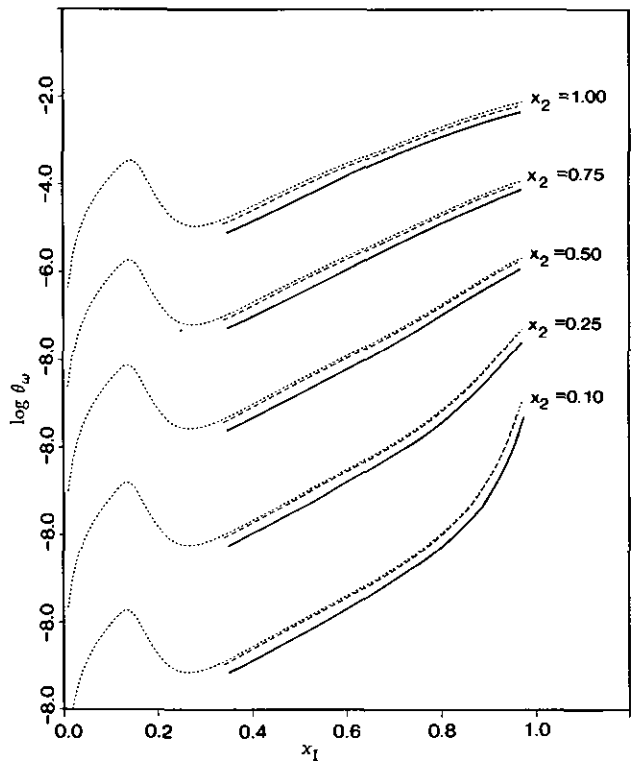

FIG. 6. Streamwise variation of the wall skew angle for the wedge flow for five selected cross-stream locations; ··· full calculation; – – – embedded-function; ——— assuming collateral wall-layer flow.

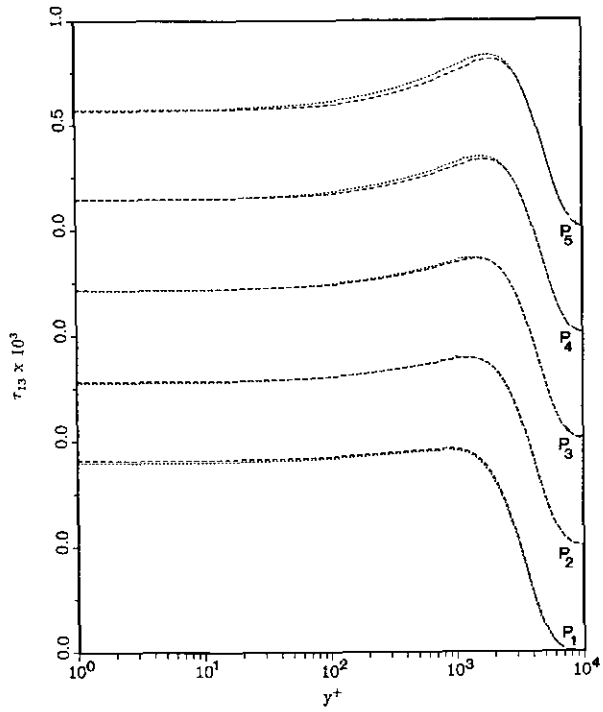

FIG. 7. The streamwise total shear stress at five selected locations. See Fig. 5 for legend.

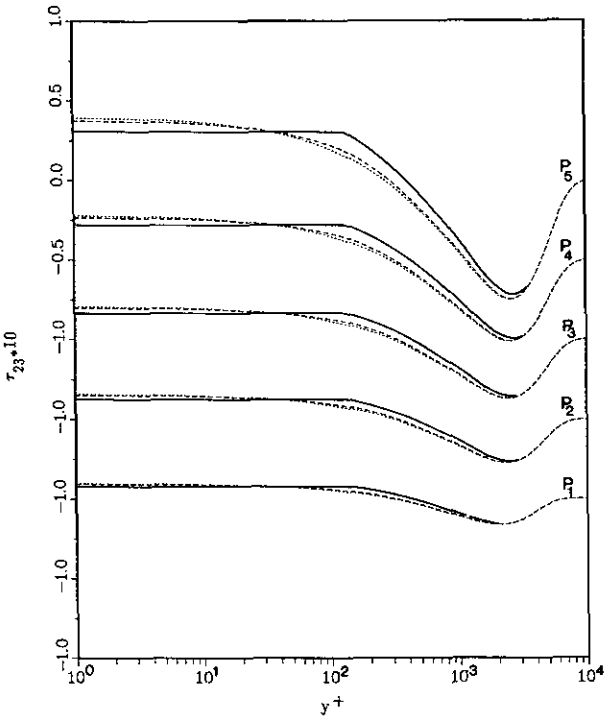

FIG. 8. The cross-stream total shear stress at five selected locations. See Fig. 5 for legend. Solid curves are results obtained assuming collateral wall-layer flow.

collateral flow). While this is a valid asymptotic result [7] in the limit $\mathrm{Re} \to \infty$, significant error may result using such an approximation at the finite but large Reynolds numbers encountered in practice and this aspect will now be assessed. The assumption of collateral flow implies that the pressure-gradient terms in (41) and (42), which give rise to the skewing of the velocity, should be neglected to obtain

$$f_3 - f_2 = \frac{u_*}{\kappa} \log\left(\frac{\eta_3}{\eta_2}\right), \qquad g_3 - g_2 = \frac{u_*^2 \theta_*}{\kappa} \log\left(\frac{\eta_3}{\eta_2}\right). \tag{59}$$

Furthermore, from (48), the scaled friction velocity and wall skew angle are now calculated from

$$u_* = \frac{f_2}{(1/\kappa)\log y^+ + C_i}, \qquad \theta_* = \frac{g_2}{u_* f_2}. \tag{60}$$

The calculations for the wedge flow were repeated assuming collateral flow in the wall layer; it was found that computed results for u_τ and δ^*, as well as the streamwise velocity and total shear stress profiles did not differ appreciably from those obtained with the FC method. However, the computed value of θ_w assuming collateral flow is consistently underpredicted, as shown in Fig. 6, with the difference from the true value corresponding to the total angle of skew of the velocity in the wall layer; percentage errors for θ_w on the order of 30% are typical using the collateral flow approach. Figures 8 and 9 show the cross-stream total shear stress and velocity profiles, respectively, obtained by assuming collateral flow in the wall layer, and it is seen that the agreement with the FC method has deteriorated considerably. It is seen from Figs. 8 and 9 that the effect of assuming collateral flow in the wall layer alters the cross-stream flow all the way to $y^+ \simeq 1000$, a location which corresponds to approximately 10 times the thickness of the wall layer. The importance of including the effects of pressure gradient on the wall-layer flow was also pointed out in another recent study [17].

As a second and more challenging example to demonstrate the applicability of the EF method to the calculation of bi-directionally skewed cross-stream profiles, consider the external velocity given by

$$U_e = 1 - \frac{2e^{-(\pi x_2)^2}}{\pi^2} \sin(2\pi x_1). \tag{61}$$

This flow has a symmetry plane at $x_2 = 0$ and asymptotes to a uniform flow for $|x_2|$ large. Furthermore, it is assumed that for the external flow: (i) $\partial u_3/\partial x_3 = 0$ as $x_3 \to 0$, and (ii) the normal component of the vorticity is zero. From the two

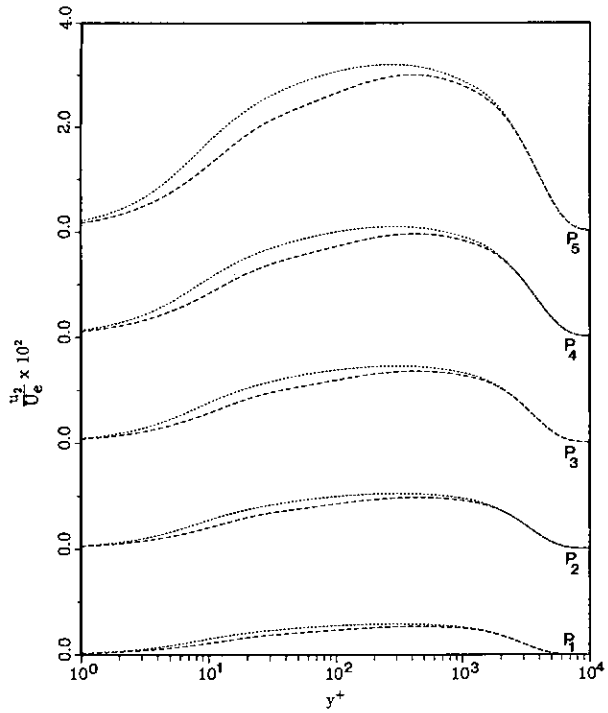

FIG. 9. The cross-stream velocity at five selected locations. Collateral wall-layer flow is assumed in the embedded-function method. See Fig. 5 for legend.

conditions above, it may be easily shown [7] that the metric coefficients can be expressed as

$$h_1 = h_2 = U_e^{-1}. \tag{62}$$

From the definitions of K_1 and K_2, in (5), it follows that

$$K_1 = \frac{\partial U_e}{\partial x_1} = -\frac{4e^{-(\pi x_2)^2}}{\pi}\cos(2\pi x_1), \tag{63}$$

$$K_2 = \frac{\partial U_e}{\partial x_2} = 4x_2 e^{-(\pi x_2)^2}\sin(2\pi x_1). \tag{64}$$

Equation (64) indicates that the curvature of the external streamline is initially positive along $0 < x_1 < 0.5$ and then negative along $0.5 < x_1 < 1.0$; this external field was constructed to have a change in sign of K_2, as this appears to be a necessary requirement for a bi-directionally skewed cross-stream velocity profile. With the external conditions specified by (61)–(64), the FC and EF methods were employed to calculate the boundary-layer flow starting from a Blasius profile along $x_1 = 0$. In addition, the reference quantities used for the wedge flow, as well as the criteria for transition, were left unchanged.

Figure 10 shows the variation of the wall skew angle as a function of x_1 for a selected number of cross-stream locations. It is evident that the calculated results from the two methods are in good agreement. From (64), it is noted that for a fixed x_2 location, the maximum, zero, and minimum values of K_2 occur at $x_1 = 0.25$, 0.5, and 0.75, respectively. The wall skew angle follows a similar trend but the maximum, zero, and minimum are approximately located at $x_1 = 0.4$, 0.6, and 0.9, respectively. This indicates a consistent lag in the response of the wall skew angle to the changing cross-stream pressure gradient in the external flow.

Figure 11 shows the cross-stream velocity profile at various streamwise locations for a fixed cross-stream location. Once again, it may be noted that the results obtained from the FC and EF methods are in good agreement. There are some noteworthy features in these plots and which merit discussion. At the first streamwise location, $x_1 = 0.4$, the cross-stream velocity profile skews in the positive x_2 direction throughout the extent of the boundary-layer, reflecting the fact that the curvature of the external streamline is positive. Farther downstream, at $x_1 = 0.6$, the magnitude of the cross-stream velocity decreases as a result of a decreasing curvature in the external streamline. At the next two locations, the cross-stream velocity profile is bi-directionally skewed which reflects the change in the sign of the curvature of the external streamline. Since the inertia of the fluid in the wall layer is smaller than that in the outer layer, the velocity profile in the wall layer responds to the

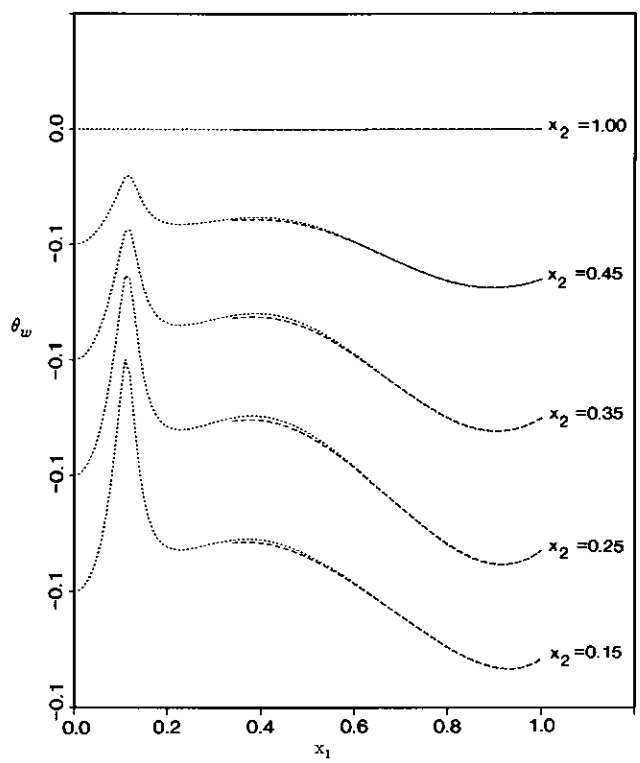

FIG. 10. Streamwise variation of the wall skew angle at five cross-stream locations: ··· full calculation; – – – embedded function.

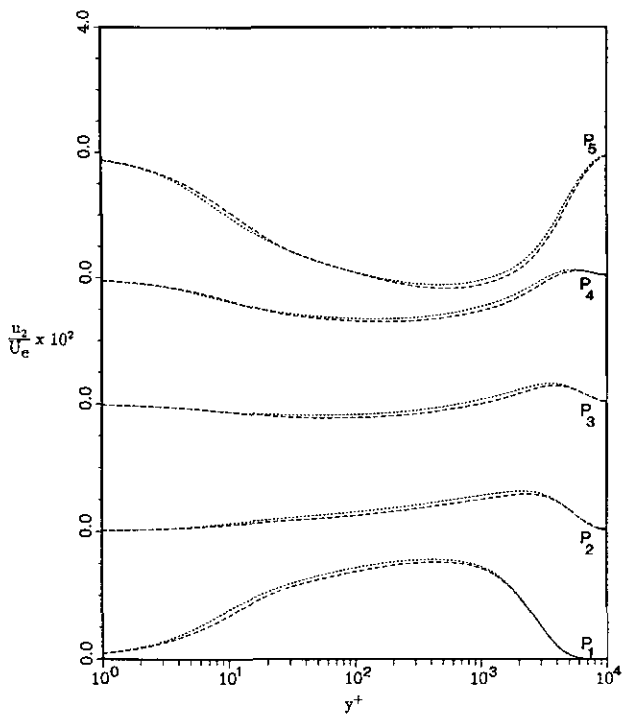

FIG. 11. The cross-stream velocity at five selected locations: ··· full calculation; – – – embedded function method. All cross-stream locations at $x_2 = 0.25$ and the streamwise locations are given by: P_1, $x_1 = 0.4$; P_2, $x_1 = 0.6$; P_3, $x_1 = 0.65$; P_4, $x_1 = 0.7$; P_5, $x_1 = 0.9$.

changing external environment relatively more rapidly. Consequently, for the two locations under discussion, the velocity in the wall layer skews in the negative x_2 direction, but the velocity in the outer layer "remembers" its upstream history and continues to skew in the positive x_2 direction. As the flow continues in the downstream direction, the changes in the wall-layer flow permeate out toward the boundary-layer edge and the maximum in the positive cross-stream velocity continually decreases. At the streamwise location of the last plot, the cross-stream velocity is once again unidirectionally skewed, but now in the negative x_2 direction, implying that the outer layer has now "forgotten" the positive curvature of the external streamline farther upstream.

7. CONCLUSIONS

The embedded-function method utilizes about half as many mesh points as are normally required in a conventional scheme which computes the flow all the way to the wall. The computed results (particularly the wall skew angle and the cross-stream velocity and shear stress profiles) were obtained by using the embedded-function method at a fraction of the computational cost and yet agree well with those obtained by the conventional scheme. It was shown that the assumption of collateral flow in the wall layer leads to inaccurate results in the prediction of the wall skew angle and the cross-stream velocity and shear stress profiles. Furthermore, it was demonstrated that the present embedded-function method is capable of calculating boundary-layer flows in which the cross-stream velocity profile is bi-directionally skewed.

It should be noted that the present methodology applies to attached turbulent flows near walls and, in principle, is readily incorporated in implicit schemes for the solution of the Reynolds-averaged Navier–Stokes equations. For attached turbulent boundary layers, the two-layer structure utilized here and the validity of the turbulence models represented by (32) are well documented. The validity of such models in and near backflow zones and regions of separation is questionable and turbulence models for these regimes will probably be controversial for some time. At the same time, if a two-layer turbulence model is adopted for separated flow, the methodology could, in principle, be extended to this situation.

APPENDIX

The variable G and coefficients A_i in the governing equations (23)–(25) are given by

$$A_1 = W\frac{Z_o}{h_1}, \qquad A_3 = \frac{W}{U_e h_1}\frac{\partial U_e}{\partial x_1},$$
$$A_8 = \frac{W}{\Delta_o h_1}\frac{\partial \Delta_o}{\partial x_1} + A_3 - A_5 \tag{A.1}$$

and by the following

Three-Dimensional	Plane of symmetry		
$G = \frac{u_2}{U_e}$	$G = \frac{1}{U_e h_2}\frac{\partial u_2}{\partial x_2}\Big\|_{x_2=0}$		(A.2)
$A_2 = \frac{W}{h_2}$	$A_2 = 0$		(A.3)
$A_4 = A_7 = WK_2$	$A_4 = WK_2'$,	$A_7 = W$	(A.4)
$A_5 = A_6 = WK_1$	$A_5 = 2WK_1$,	$A_6 = 0$	(A.5)
$A_9 = \frac{W}{\Delta_o h_2}\frac{\partial \Delta_0}{\partial x_2}$	$A_9 = W$,		(A.6)

where

$$W = U_e \Delta_o^2, \qquad K_2' = \frac{1}{h_2}\frac{\partial K_2}{\partial x_2}\Big|_{x_2=0}. \tag{A.7}$$

ACKNOWLEDGMENTS

The authors gratefully acknowledge support from NASA Lewis Research Center under Grant NAG 3-771 and the Air Force Office of Scientific Research under Grant 89-0487.

REFERENCES

1. O. L. Anderson, United Technologies Research Center Report No. CR174894, 1985 (unpublished).
2. O. L. Anderson, *J. Fluids Eng.* **109**, 41 (1987).
3. Y.-S. Wie and F. R. DeJarnette, AIAA Paper 88-0617, Reno, NV, 1988 (unpublished).
4. J. D. A. Walker, M. C. Ece, and M. J. Werle, *AIAA J.* **29**, 1810 (1991).
5. A. T. Degani and J. D. A. Walker, AIAA Paper 90-0307, AIAA 28th Aerospace Sciences Meeting, Reno, NV, 1990, unpublished.
6. M. R. Rubesin and J. R. Viegas, "A Critical Examination of the Use of Wall Functions as Boundary Conditions in Aerodynamic Calculations," Third Symposium on Numerical and Physical Aspects of Aerodynamic Flows, California State University, Long Beach, CA, 1985.
7. A. T. Degani, Ph.D. thesis, Lehigh University, 1991 (unpublished).
8. A. T. Degani, F. T. Smith, and J. D. A. Walker, *J. Fluid Mech.* **234**, 329 (1992).
9. A. T. Degani, F. T. Smith, and J. D. A. Walker, *J. Fluid Mech.* **250**, 43 (1993).
10. J. D. A. Walker, D. E. Abbott, R. K. Scharnhorst, and G. G. Weigand, *AIAA J.* **27**, 140 (1989).
11. V. N. Vatsa and R. T. Davis, NASA CR-112315, 1973.
12. T. Cebeci and A. M. O. Smith, *Analysis of Turbulent Boundary Layers* (Academic Press, New York, 1974).
13. S. Dhawan and R. Narasimha, *J. Fluid Mech.* **3**, 418 (1958).
14. F. M. White, *Viscous Fluid Flow* (McGraw–Hill, New York, 1974).
15. F. T. Smith and J. Gajjar, *J. Fluid Mech.* **144**, 191 (1984).
16. U. Goldberg and E. Reshotko, *AIAA J.* **22**, 914 (1984).
17. R. W. Barnwell, "Nonadiabatic and Three-Dimensional Effects in Compressible Turbulent Boundary Layers," *AIAA J.* **30**, 897 (1992).